

 Open access • Journal Article • DOI:10.1039/C8QI00703A

Realizing a stable high thermoelectric $zT \sim 2$ over a broad temperature range in Ge_{1-x-y}Ga_xSb_yTe via band engineering and hybrid flash-SPS processing

— [Source link](#) 

Bhuvanesh Srinivasan, Bhuvanesh Srinivasan, Alain Gellé, Francesco Gucci ...+6 more authors





Institutions: Queen Mary University of London, University of Rennes

Published on: 15 Jan 2019 - Inorganic chemistry frontiers (The Royal Society of Chemistry)

Topics: Fermi level, Seebeck coefficient, Effective mass (solid-state physics), Thermoelectric effect and Atmospheric temperature range

Related papers:

- [High-performance bulk thermoelectrics with all-scale hierarchical architectures](#)
- [Rhombohedral to Cubic Conversion of GeTe via MnTe Alloying Leads to Ultralow Thermal Conductivity, Electronic Band Convergence, and High Thermoelectric Performance](#)
- [Impact of Coinage Metal Insertion on the Thermoelectric Properties of GeTe Solid-State Solutions](#)
- [Realizing \$zT\$ of 2.3 in Ge_{1-x-y}Sb_xIn_yTe via Reducing the Phase-Transition Temperature and Introducing Resonant Energy Doping.](#)
- [Resonant level-induced high thermoelectric response in indium-doped GeTe](#)

Share this paper:    

View more about this paper here: <https://typeset.io/papers/realizing-a-stable-high-thermoelectric-zt-2-over-a-broad-zfj87vp458>

Realizing a Stable High Thermoelectric $zT \sim 2$ over a Broad Temperature Range in $\text{Ge}_{1-x-y}\text{Ga}_x\text{Sb}_y\text{Te}$ via Band Engineering and Hybrid Flash-SPS Processing

Bhuvanesh Srinivasan^{a,b,*}, Alain Gellé^c, Francesco Gucci^b, Catherine Boussard-Pledel^a, Bruno Fontaine^a, Régis Gautier^a, Jean-François Halet^{a,*}, Michael J. Reece^b and Bruno Bureau^a

^a University of Rennes, Ecole Nationale Supérieure de Chimie de Rennes, CNRS, ISCR – UMR 6226, F-35000 Rennes, France.

^b School of Engineering and Materials Science, Queen Mary University of London, London E1 4NS, United Kingdom.

^c University of Rennes, CNRS, IPR – UMR 6251, F-35000 Rennes, France.

* Correspondence – bhuvanesh.srinivasan@univ-rennes1.fr; jean-francois.halet@univ-rennes1.fr

Abstract – We report a remarkably high and stable thermoelectric figure of merit, zT close to 2 by manipulating the electronic bands in Ga-Sb codoped GeTe, which has been processed by hybrid flash-spark plasma sintering. According to the experimental results and first-principles calculations, the vast enhancement achieved in the thermopower due to codoping of Ga (2 mol%) and Sb (8 mol%) in GeTe is attributed to a concoction of reasons: (i) suppression of hole concentration; (ii) improved band convergence by decreasing the energy separation between the two valence band maxima to 0.026 eV; (iii) Ga predominantly contributing to the top of the valence band in Ga-Sb codoped GeTe, despite Ga-induced resonance state not located at a favorable position near the Fermi level; (iv) active participation of several bands increasing the hole carrier effective mass; (v) facilitating band degeneracy by reducing the $R3m \rightarrow Fm-3m$ structural transition temperature from 700 K to 580 K. The synergy between these complementary and beneficial effects, in addition to the reduced thermal conductivity, enabled the flash sintered $\text{Ge}_{0.90}\text{Ga}_{0.02}\text{Sb}_{0.08}\text{Te}$ composition to not only exhibit a peak of zT of ~ 1.95 at 723 K, but also to maintain/stabilize its high performance over a broad range of temperature (600 – 775K), thus making it a serious candidate for mid-temperature range energy harvesting devices.

1. Introduction

Within the realms of exploring alternative means to power the planet, the requirement to generate and store energy sustainably represents one of the critical challenges across the boundaries of the science and technology in the 21st century. In this regard, thermoelectric (TE) materials and devices have drawn increasing interest and attention due to their potential to reversibly convert waste heat into fruitful electricity. A TE material's efficiency is generally quantified by the dimensionless figure of merit defined as $zT = S^2\sigma T/\kappa_{total}$ where S , σ , T and κ_{total} are the Seebeck coefficient, electrical conductivity, temperature and total thermal conductivity (sum of the electronic part, κ_e , and the lattice part, κ_{latt}), respectively. The main paradigm to achieve high zT in materials is to enhance their power factor ($S^2\sigma$) and/or reduce their thermal transport properties (κ_{total}). Most of the TE research activities are aimed at reducing κ_{latt} to enhance zT by phonon scattering due to nanostructuring¹⁻³, intrinsic bond anharmonicity⁴⁻⁶, rattling impurities⁷, etc. However, S and σ are highly intertwined and present a greater challenge in enhancing the power factor, paramount for better energy conversion efficiency. Advances in recent times have shown that the concept of 'band structure engineering', which includes convergence of electronic band valleys,^{8,9} quantum confinement of electron charge carriers,¹⁰ electron filtering,¹¹ inducing resonant levels by impurities near the Fermi level,¹² nestification,¹³ dimensionality reduction,¹⁴ deformation potential coefficient,¹⁵ and effective mass,¹⁶ are effective in decoupling S and σ to a certain

extent. Even the idea of semiconducting chalcogenide glasses (based on phonon-glass electron-crystal approach) as potential thermoelectric materials have been tried with varying degree of success.^{17–20}

Though the concept of band engineering is extensively applied to various *p*- and *n*-type materials like SnTe^{21–25}, PbTe^{26–28}, half-Heuser²⁹ and Mg₂Si³⁰, it is applied relatively less on GeTe-based materials. Some of the strategies for GeTe based materials to enhance the power factor and/or to suppress κ_{latt} have been adopted on compositions such as GeTe-AgSbTe₂ (TAGS),³¹ GeTe-LiSbTe₂,³² GeTe-AgInTe₂,³³ GeTe-AgSbSe₂,³⁴ (GeTe)_nSb₂Te₃,³⁵ Ge_{1-x}Pb_xTe,³⁶ Ge_{1-x}Bi_xTe,³⁷ (Bi₂Te₃)_nGe_{1-x}Pb_xTe,³⁸ Ge_{1-x}In_xTe,³⁹ GeTe_{1-x}Se,⁴⁰ Ge_{1-x}Sb_xTe,^{41,42} Ge_{1-x}Ag_xTe,⁴³ Ge_{1-x}Mn_xTe,^{44,45} Ge_{1-x-y}Sn_xPb_yTe,⁴⁶ Ge_{1-x}Sb_xTe_{1-y}Se_y,⁴⁷ GeTe-GeSe-GeS,⁴⁸ Ge_{1-x-y}Bi_xSb_yTe,⁴⁹ Ge_{1-x-y}Bi_xIn_yTe²⁵ and more recently Ge_{0.9-y}Pb_{0.1}Bi_yTe.⁵⁰ The crystal structure of GeTe-based compounds undergoes a second-order ferroelectric structural transition from rhombohedral symmetry (low temperature phase) to cubic symmetry (high temperature phase) at around 700 K.⁵¹ Motivated by the results of Wu *et al.* on Ge_{1-x}In_xTe,³⁹ showing that the introduction of resonant levels in the vicinity of the Fermi level due to indium doping leads to a reasonably high *zT* in GeTe (*zT* ~ 1.3 at 630 K), we here have tried to explore the effect of another group 13 element, namely Ga on the TE performance of GeTe. From the latest work on Ge_{1-x-y}Bi_xSb_yTe,⁴⁹ it was also established that 8-10 mol% Sb doping in GeTe helped to improve the band degeneracy by pushing the system towards the cubic structure (c-GeTe). Hence aiming at bringing in synergistic band effects, we investigated the effect of codoping of Ga and Sb on the structural, electronic and thermoelectric properties of GeTe. As group 13 elements and Sb have distinctive roles, we expect codoping of Ga and Sb in GeTe to result in a synergistic band effect, i.e., cumulative effect of resonant states induced by Ga and band degeneracy caused by Sb, which ultimately should increase the thermopower of the material.

Compounds with the nominal compositions of Ge_{1-x}Ga_xTe (*x* = 0.00 – 0.10) were synthesized by vacuum-sealed tube melt processing, followed by consolidation by Spark Plasma Sintering (SPS). The optimum content of resonant states was achieved when 2 mol% Ga was substituted for Ge in GeTe. Indeed, this substitution marginally improved the thermoelectric performance (*zT* ~ 1.1 at 720 K) when compared to pristine GeTe (*zT* ~ 0.95 at 720 K). Further, when 8-10 mol% Sb was codoped to Ge_{0.98}Ga_{0.02}Te, we successfully realized the co-adjuvant synergistic band effects in GeTe. Thus, the Ge_{0.88}Ga_{0.02}Sb_{0.10}Te composition with a high thermopower and ultra-low κ_{total} manifested a maximum *zT* ~ 1.75 at 725 K, which was 80% higher than that of pristine GeTe. With the state-of-the art ‘hybrid flash-SPS’ processing,^{52,53} this *zT* value was further improved to ~ 2 at 725 K (more than 100% improvement when compared to undoped GeTe). Interestingly, this high value of *zT* is notably maintained over a broad temperature range (600 – 775 K). The results obtained for Ge_{1-x}Ga_xTe (*x* = 0.00 – 0.10) are first discussed, followed by Ge_{1-x-y}Ga_xSb_yTe (*x* = 0.02; *y* = 0.08 – 0.10). Note that all results are presented together in the same figures and tables for a better comparison. Owing to their meager TE properties, the results of Ge_{0.90}Ga_{0.10}Te are given in Supporting Info (SI).

2. Materials & Methods

Reagents

Ge (Umicore, 99.999%), Sb (Alfa Aesar, 99.999%), Ga (Alfa Aesar, 99.999%) and Te (JGI, 99.999%) were used for synthesis without any further purification.

Synthesis

Samples of Ge_{1-x}Ga_xTe (*x* = 0.00 – 0.07) and Ge_{1-x-y}Ga_xSb_yTe (*x* = 0.02; *y* = 0.08, 0.10) were synthesized using the vacuum-sealed tube melt processing. Appropriate stoichiometric amounts of the starting elements of

Ge, Ag and Te were introduced into a fused silica tube that had previously been cleaned with hydrofluoric (HF) acid and distilled water and dried under vacuum. The ampoules were sealed under a vacuum of 10^{-6} Torr, then placed in a rocking furnace and slowly heated up to 950 °C over a period of 12 hours, then held at that temperature for 12 hours and slowly cooled down to room temperature. The obtained ingots were crushed and milled. The powders were then consolidated by SPS (FCT Systeme GmbH) at 723 K (heating rate ~ 80 °C/min) for 5 mins (holding time) under an axial pressure of 85 MPa. The sample with better TE properties was also consolidated by ‘Hybrid’ Flash-SPS processing, where the powders were sintered at 893 K and a heating rate of $\sim 10,000$ °C/min (heated from 293 – 893 K in 3 seconds) under an axial pressure of 55 MPa. More information regarding this processing technique is provided in SI. The schematics of the experimental set-up and the current flow paths for SPS (graphite punches and die), Flash-SPS (graphite punches and no die) and Hybrid Flash-SPS (graphite punches and a thin walled stainless steel die) configurations are compared and explained in SI (Figure S1 and Table S1). Highly dense disk-shaped pellets were obtained with theoretical densities of 100% for SPS and $\sim 98\%$ for Hybrid Flash-SPS. The obtained ingots and sintered discs were cut and polished to the required shapes and dimensions for various thermoelectric measurements.

Powder X-ray diffraction

X-ray diffraction (XRD) patterns were recorded at room temperature in the 2θ range 15-120° with a step size of 0.026° and a scan time per step of 400 s using a PANalytical X’Pert Pro diffractometer (Cu $K-L_{2,3}$ radiation, $\lambda = 1.5418$ Å, PIXcel 1D detector).

Hall measurements

The Hall measurements were carried out at room temperature using a home-made four-point probe setup (van der Pauw method), where a fixed magnetic field of 0.112 T and a dc current of 15 mA were applied. The measurements were made on square-shaped samples of dimensions $\sim 5 \times 5 \times 2$ mm³. The carrier concentration (n) and mobility (μ) were computed using the following equations,

$$n_s = n \times t = \frac{IB}{e|V_H|} \quad (1)$$

$$\mu = 1/(en_s R_s) \quad (2)$$

where n_s , R_s , V_H , e , B , I and t are the carrier sheet density, sheet resistance, Hall Voltage, charge of the electron, magnetic field, current and thickness of the sample, respectively. The values of carrier density obtained were quite consistent with an error of less than 2%.

Electrical and thermal transport

For each sample, the electrical resistivity and Seebeck coefficient was measured simultaneously from room temperature to 723 K using a commercial instrument (LSR-3, Linseis Inc.), in He atmosphere. The measurements were made on rectangular samples of dimension $\sim 10 \times 2 \times 2$ mm³.

The thermal diffusivity, D , was measured from room temperature to 723 K using the laser flash diffusivity method in a Netzsch LFA-457 instrument. Disc-shaped samples of 10 mm diameter and ~ 2 mm thickness were used for the measurements. The temperature dependent heat capacity, C_p , was derived using the Dulong–Petit relation as in equation (3),

$$C_p = 3R/M \quad (3)$$

where R is the gas constant and M is the molar mass.

The total thermal conductivity κ_{total} was calculated using equation (4),

$$\kappa_{total} = DC_p\rho \quad (4)$$

where ρ is the density of the sample. The density of the discs was measured using Archimedes' principle.

To better understand the thermal transport properties, the contributions from electronic and lattice parts were calculated. The lattice thermal conductivity (κ_{latt}) was estimated from κ_{total} by subtracting the electronic contribution (κ_e) via Wiedemann-Franz law, as in equation (5),

$$\kappa_e = L\sigma T \quad (5)$$

where κ_e is the electronic thermal conductivity and L is the Lorenz number computed by the condensed version of Single Parabolic Band model with acoustic phonon scattering (SPB-APS)^{54,55}, as in equation (6)

$$L = 1.5 + \exp\left[-\frac{|S|}{116}\right] \quad (6)$$

where Seebeck coefficient (S) is in μVK^{-1} and Lorenz number (L) is in $10^{-8} \text{W}\Omega\text{K}^{-2}$.

The uncertainty in the results for the values of electrical and thermal transport properties was $\sim 5\%$ and $\sim 7\%$, respectively and for the overall zT was $\sim 12\%$. Error bars are not shown in the figures to increase readability.

Computational procedures

Density Functional Theory (DFT) calculations were performed to understand the effect of doping on the electronic states. We used the projector-augmented-wave (PAW) approach⁵⁶ implemented in the Vienna ab initio simulation package (VASP)⁵⁷. Calculation were performed using generalized gradient approximation (GGA) for the exchange-correlation term parametrized by Perdew et al.⁵⁸ Spin orbit coupling was also included in the computations.

As we were interested in high temperature behavior of doped GeTe, calculations were performed on the cubic structural models. Impurities were substituted to Ge atom in a $4 \times 4 \times 4$ super-cell. Considering the previous study by Hoang *et al.*⁵⁹ on the impurity clustering in GeTe, we adopted a cluster of one Ga atom surrounded by 6 Sb atoms (second neighbors) for the Ga-Sb codoped GeTe composition ($\text{Sb}_6\text{GaGe}_5\text{Te}_{64}$). In order to understand the relative effect of both atoms, the calculations were also performed for $\text{GaGe}_{63}\text{Te}_{64}$ and $\text{Sb}_6\text{Ge}_{58}\text{Te}_{64}$ models. In all the three cases, the positions were fully relaxed. For the irreducible cell, the Brillouin-zone integration was performed using a $25 \times 25 \times 25$ Monkhorst-Pack k -mesh. For the super cell, we used a $3 \times 3 \times 3$ k -mesh for the atom relaxation and a $7 \times 7 \times 7$ k -mesh for the DOS calculations.

The carrier effective mass (m^*) was derived for each sample using a single parabolic band model^{60,61} and the measured room temperature Seebeck coefficient (S) and carrier concentration (n). The chemical potential (μ) was estimated using equation (7) with $\lambda = 0$ (acoustic-phonon scattering), where $F_j(\mu)$ is the Fermi integrals given by equation (8). The hole effective mass can then be determined from equation (9).

$$S = \frac{K_B}{e} \left\{ \frac{(2 + \lambda)F_{1+\lambda}(\mu)}{(1 + \lambda)F_\lambda(\mu)} - \mu \right\} \quad (7)$$

$$F_j(\mu) = \int_0^\infty \frac{\xi^j d\xi}{1 + e^{(\xi - \mu)}} \quad (8)$$

$$m^* = \frac{h^2}{2k_B T} \left[\frac{n}{4\pi F_{1/2}(\mu)} \right]^{2/3} \quad (9)$$

3. Results & Discussion

Sharp reflections from powder XRD indicated the good crystalline nature of all of the synthesized ingots (Figure 1). All of the main reflections could be indexed to a rhombohedral GeTe phase (PDF#47-1079, $R3m$ space group). The rhombohedral phase was further confirmed by the presence of double reflections [(024) and (220)] in the range of 2θ values between 41° to 44° in $\text{Ge}_{1-x}\text{Ga}_x\text{Te}$. Minor reflections of Ge impurities could be detected in some samples, which could be due to intrinsic Ge vacancies, as GeTe always prefers to have a Te-rich composition, as in agreement with the previous experiments.^{43,49,62}

Holes were the major charge carriers (p -type), as the Hall voltage was positive in these samples. The results from Hall measurements are presented in Table 1. The carrier concentration value at room temperature decreased with increasing Ga content. In pristine GeTe, the Ge vacancy has a very low formation energy and is the most easily formed intrinsic defects.^{62,63} The addition of Ga to GeTe can suppress these Ge vacancies, thereby leading to a reduction in the density of charge carriers. In most cases, the carrier mobility, μ , will increase with the decreasing charge carrier density. However, the mobility values in $\text{Ge}_{1-x}\text{Ga}_x\text{Te}$ had a contrasting effect, where they consistently reduced with increasing Ga content. This reduction in mobility with Ga content can be due to the increased density of ionized impurities and/or alloy scattering. Such mobility reductions are commonly observed in materials with group 13 dopants.^{12,39}

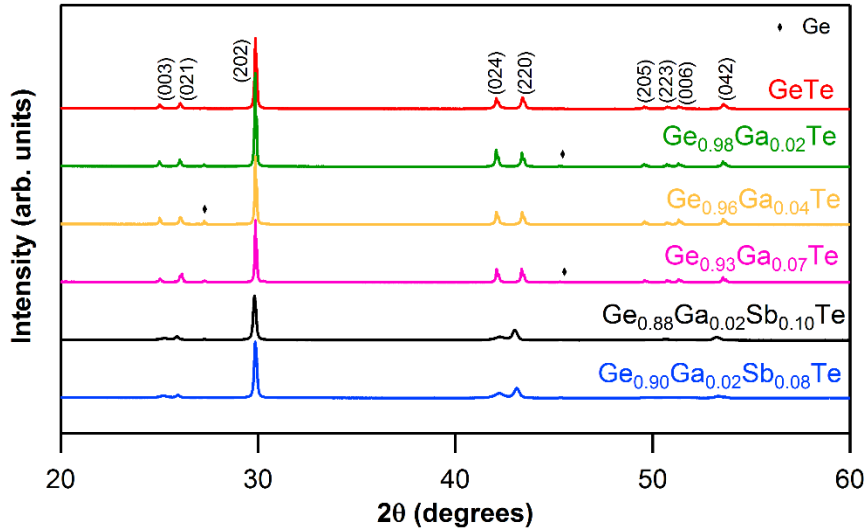


Figure 1. Powder XRD patterns for $\text{Ge}_{1-x}\text{Ga}_x\text{Te}$ ($x = 0$ to 0.07) and $\text{Ge}_{1-x-y}\text{Ga}_x\text{Sb}_y\text{Te}$ ($x = 0.02$; $y = 0.08, 0.10$) samples.

Table 1. Hall measurement results (at ~ 300 K) of carrier concentration, mobility, and computed effective mass for $\text{Ge}_{1-x}\text{Ga}_x\text{Te}$ ($x = 0.00 - 0.07$) and $\text{Ge}_{1-x-y}\text{Ga}_x\text{Sb}_y\text{Te}$ ($x = 0.02$; $y = 0.08, 0.10$) samples.

Sample	Carrier Concentration, n (cm^{-3})	Mobility, μ ($\text{cm}^2\text{V}^{-1}\text{s}^{-1}$)	Effective mass, m^*
GeTe	9.08×10^{20}	57.01	$1.30m_e$

$\text{Ge}_{0.98}\text{Ga}_{0.02}\text{Te}$	8.73×10^{20}	51.76	$1.72m_e$
$\text{Ge}_{0.96}\text{Ga}_{0.04}\text{Te}$	7.85×10^{20}	43.72	$1.64m_e$
$\text{Ge}_{0.93}\text{Ga}_{0.07}\text{Te}$	6.35×10^{20}	32.04	$1.65m_e$
$\text{Ge}_{0.88}\text{Ga}_{0.02}\text{Sb}_{0.10}\text{Te}$	1.83×10^{20}	29.65	$1.97m_e$
$\text{Ge}_{0.90}\text{Ga}_{0.02}\text{Sb}_{0.08}\text{Te}$	3.96×10^{20}	29.82	$2.38m_e$
$\text{Ge}_{0.90}\text{Ga}_{0.02}\text{Sb}_{0.08}\text{Te}$ by hybrid flash-SPS	2.13×10^{20}	35.81	$2.03m_e$

The electrical conductivity of all of the samples decreased with temperature (Figure 2a), which is the archetypal behavior of degenerate semi-conductors. The Ga-doping systematically increased the electrical resistance, a reflection of the cumulative effect of deflation in both the charge carrier density and mobility with Ga content. The Seebeck coefficient, S , was positive for all the composition over the entire temperature range (Figure 2b). This indicated p -type charge carriers, consistent with the Hall measurement results. With the increasing Ga content, there was a notable improvement in S values both at room temperature and at higher temperature for $\text{Ge}_{1-x}\text{Ga}_x\text{Te}$ samples. This modest improvement in S values can be attributed to the suppression of the carrier concentration by Ga doping. The temperature dependence of the power factors ($S^2\sigma$) are shown in Figure 2c for $\text{Ge}_{1-x}\text{Ga}_x\text{Te}$ samples. Comparing pristine GeTe, there was a marginal but significant improvement in the power factor for the 2 mol% Ga doped sample, which exhibited a maximum power factor of $\sim 4.1 \times 10^{-3} \text{ W/mK}^2$ at 720 K. The advantage of an improved power factor in GeTe by 2 mol% Ga doping was maintained across the measured temperatures. The power factors of other $\text{Ge}_{1-x}\text{Ga}_x\text{Te}$ samples for $x > 0.02$ were lower than the undoped sample. Hence in $\text{Ge}_{1-x}\text{Ga}_x\text{Te}$ system, the optimized value of $x = 0.02$ provided the needed proper trade-off between the electrical transport properties.

ACCEPTED

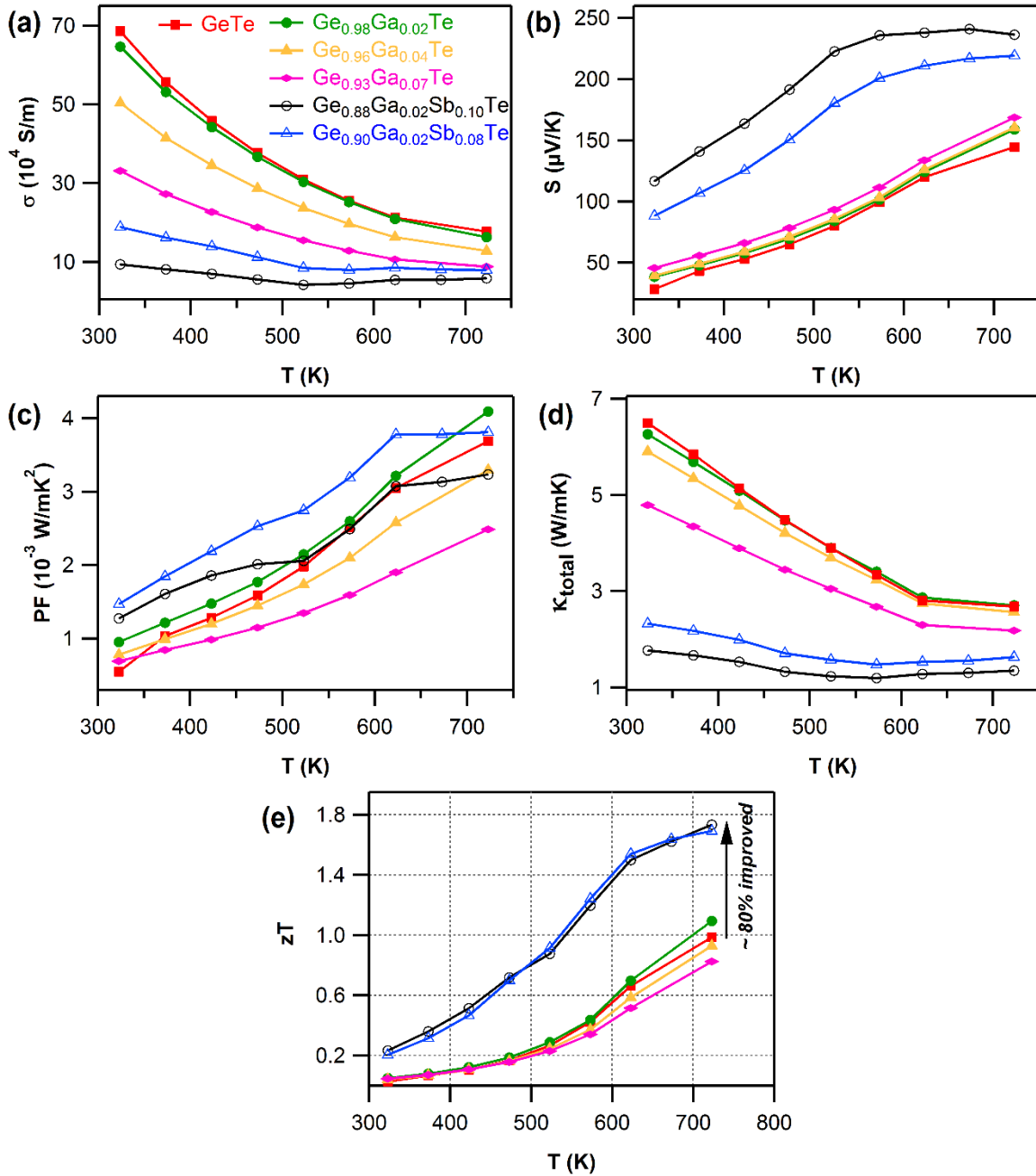


Figure 2. Temperature-dependent (a) electrical conductivity (σ), (b) Seebeck coefficient (S), and (c) power factor ($\text{PF} = S^2\sigma$), (d) total thermal conductivity (κ_{total}), (e) figure of merit (zT) for $\text{Ge}_{1-x}\text{Ga}_x\text{Te}$ ($x = 0.00 - 0.07$) and $\text{Ge}_{1-x-y}\text{Ga}_x\text{Sb}_y\text{Te}$ ($y = 0.02$; $z = 0.08, 0.10$) samples.

The total thermal conductivity, κ_{total} (Figure 2d), monotonically decreased with Ga content in $\text{Ge}_{1-x}\text{Ga}_x\text{Te}$ samples. The contributions from electronic (κ_e) and lattice (κ_{latt}) parts are presented in SI (Figure S5). The temperature dependent Lorenz number, L obtained by fitting their respective Seebeck coefficients for the samples of $\text{Ge}_{1-x}\text{Ga}_x\text{Te}$ were in the range of 2.3×10^{-8} to 1.8×10^{-8} $\text{W}\Omega\text{K}^{-2}$ and lower than the metallic limit of 2.45×10^{-8} $\text{W}\Omega\text{K}^{-2}$ (SI, Figure S4). In the case of $\text{Ge}_{1-x}\text{Ga}_x\text{Te}$, the majority of the

thermal contribution came from κ_e , which conspicuously decreased with Ga content. κ_{latt} of the Ga-doped samples were larger than that of the pristine GeTe, and this can arise when the estimation of L value cannot properly account for the electronic contribution to the thermal conductivity, as similarly observed for previously reported PbTe and SnTe based materials.^{64,65}

The maximum thermoelectric figure of merit, zT , (Figure 2e) achieved within the $\text{Ge}_{1-x}\text{Ga}_x\text{Te}$ ($x = 0.00$ to 0.10) series was ~ 1.1 at 720 K for $\text{Ge}_{0.98}\text{Ga}_{0.02}\text{Te}$, which was marginally higher than that of pristine GeTe ($zT \sim 0.95$ at 720 K). The zT values systematically decreased for the value of $x > 0.02$ in the $\text{Ge}_{1-x}\text{Ga}_x\text{Te}$ system. Heavily Ga-doped sample ($x = 0.10$) exhibited the lowest zT (SI, Figure S6), due to its high electrical resistivity arising from severe deflation of carrier concentration and mobility. Based on this evidence, it was concluded that 2 mol% Ga doping was optimum to achieve a better trade-off between S , σ and κ_{total} in the $\text{Ge}_{1-x}\text{Ga}_x\text{Te}$ ($x = 0.00$ to 0.10) series. The first-principles (density functional theory (DFT) type) calculations reported later in this paper suggests that resonant states are induced.

It has been reported that 8-10 mol% Sb doping in GeTe significantly helped to achieve band degeneracy.⁴⁹ To further improve the thermoelectric performance of $\text{Ge}_{0.98}\text{Ga}_{0.02}\text{Te}$, Sb was codoped to it to form the $\text{Ge}_{1-x-y}\text{Ga}_x\text{Sb}_y\text{Te}$ ($x = 0.02$; $y = 0.08, 0.10$) series, with an objective to bring in synergistic band effects that would help to improve the TE performance.

As observed from the XRD patterns (Figure 1), the double reflections [(024) and (220)] in the range of 2θ values between 41° to 44° , characteristics of the rhombohedral phase, got closer and almost merged when Sb was codoped into $\text{Ge}_{1-x}\text{Ga}_x\text{Te}$. As the atomic radii of Ga (1.36 Å) and Sb (1.33 Å) are larger compared to that of Ge (1.25 Å), the codoping of Ga-Sb has relaxed the rhombohedral structure of GeTe and has pushed the system towards the cubic structure. In other words, Ga-Sb codoping has promoted a faster structural transition ($R3m \rightarrow Fm-3m$) in GeTe. This was proven by the DSC data (SI, Figure S2), where the structural transition temperature was conspicuously reduced from ~ 630 K for $\text{Ge}_{0.98}\text{Ga}_{0.02}\text{Te}$ to ~ 580 K for $\text{Ge}_{0.88}\text{Ga}_{0.02}\text{Sb}_{0.10}\text{Te}$. Considering that the transition temperature for pristine GeTe is ~ 700 K, the codoping of Ga and Sb has tremendously reduced the phase transition temperature and has increased the cubic nature of the sample. From the band structure features of rhombohedral (r) and cubic (c) GeTe, it was shown that the later has a larger total band degeneracy.⁶⁶

Because of the combined actions of Ga and Sb at the Ge site in GeTe, an effective suppression of the intrinsic Ge vacancies could take place, which was reflected in the major reduction of the carrier concentration in the codoped samples (Table 1). Obviously, this contributed to the decline in σ for Ga-Sb codoped samples (Figure 2a). But this was well compensated by the large increase in the Seebeck coefficient (Figure 2b). The Ga-Sb codoped sample of composition $\text{Ge}_{0.88}\text{Ga}_{0.02}\text{Sb}_{0.10}\text{Te}$ exhibited a high thermopower of $\sim 120 \mu\text{V/K}$ at room temperature and a maximum of $\sim 240 \mu\text{V/K}$ at higher temperatures, an improvement by 70% when compared to pristine GeTe. It is also key to note that the S values of the codoped samples increased steeply till 550 K and almost became constant after that. Such a trend once again was a clear indication of the second order structural transition ($R3m \rightarrow Fm-3m$).

The increased electrical resistivity, due to the lowering of carrier density and mobility has immensely reduced the electronic contribution to thermal transport in the Ga-Sb codoped samples (SI, Figure S5a). This has led to an ultra-low κ_{total} ($< 1.3 \text{ W/mK}$ at $T > 500 \text{ K}$) in the $\text{Ge}_{1-x-y}\text{Ga}_x\text{Sb}_y\text{Te}$ samples (Figure 2d). At room temperature, $\text{Ge}_{0.88}\text{Ga}_{0.02}\text{Sb}_{0.10}\text{Te}$ sample exhibited a $\kappa_{total} \sim 1.75 \text{ W/mK}$, which accounted for a reduction by 270% when compared to pristine GeTe ($\kappa_{total} \sim 6.5 \text{ W/mK}$ at room temperature).

The combined beneficial effects of improved thermopower and reduced thermal transport, achieved by Ga-Sb codoping of GeTe, has strikingly enhanced the thermoelectric figure of merit (Figure

2e). The Ga-Sb codoped GeTe samples (both $\text{Ge}_{0.88}\text{Ga}_{0.02}\text{Sb}_{0.10}\text{Te}$ and $\text{Ge}_{0.90}\text{Ga}_{0.02}\text{Sb}_{0.08}\text{Te}$ compositions) manifested a high $zT \sim 1.75$ at 730 K, an improvement by 80% compared to undoped GeTe, and is notably one of the highest reported among the GeTe-based materials.

To have a more cogent understanding on the effects of doping in GeTe, DFT calculations were performed (see SI for the computational details). As we are interested in the high temperature domain for thermoelectric applications, these DFT calculations were carried out on $4 \times 4 \times 4$ supercells derived from the cubic structural arrangement of GeTe. The electronic densities of states (DOS) computed for the cubic models of GeTe and $\text{Ge}_{0.98}\text{Ga}_{0.02}\text{Te}$ are presented and compared in Figure 3a. As expected, the presence of some amount of Ga in GeTe, shifted the Fermi level towards the valence band. The DOS was clearly modified near the top of the valence band with respect to that of GeTe, distinctly indicated by the presence of a sharp hump near the Fermi level (E_F). This firmly establishes that Ga doping induces resonant states or deep defect states near E_F in the electronic band structure of GeTe. According to Mott's relationship,⁶⁷ the modified DOS obtained by resonant levels may contribute to an improvement in the Seebeck coefficient. This explains the marginal raise in thermopower for $\text{Ge}_{1-x}\text{Ga}_x\text{Te}$ at high temperatures (cubic phase). However, the power factor and zT were improved only for the $\text{Ge}_{0.98}\text{Ga}_{0.02}\text{Te}$ composition, while they were reduced for higher dopant content of Ga in $\text{Ge}_{1-x}\text{Ga}_x\text{Te}$ ($x > 0.02$). This happens because the distortion of DOS (resonant states) hinders electrical conductivity (owing to reduced mobility). At higher dopant levels of Ga (> 2 mol%), the DOS of the samples are modified heavily, which was reflected in their poor TE performance due to their decreased σ and μ values. Hence, the 2 mol% Ga doping in GeTe produced the optimum distortion of the DOS to notably increase the thermopower without compromising much the electrical conductivity in $\text{Ge}_{1-x}\text{Ga}_x\text{Te}$. It seems that the Ga-induced resonance level becomes more prominent only at the high temperature cubic phase, as there was not much significant change in the room temperature value of Seebeck coefficient when 2 mol% Ga was doped to GeTe.

To simulate 8-10 mol% Sb doping in GeTe, six Sb atoms were substituted for Ge in GeTe leading to the $\text{Sb}_6\text{Ge}_{58}\text{Te}_{64}$ ($\text{Sb}_{0.09}\text{Ge}_{0.91}\text{Te}$) composition. Among the different possible Sb distributions, that with Sb aggregation (i.e., Sb atoms close to each other) was considered to be the most thermodynamically stable.³⁶ Computed DOS for this Sb doped ($\text{Sb}_6\text{Ge}_{58}\text{Te}_{64} = \text{Sb}_{0.09}\text{Ge}_{0.91}\text{Te}$) composition and for the Ga-Sb codoped ($\text{GaSb}_6\text{Ge}_{57}\text{Te}_{64} = \text{Ga}_{0.02}\text{Sb}_{0.09}\text{Ge}_{0.89}\text{Te}$) GeTe (cubic) compositions are presented in Figure 3b and c, respectively. Substituting in a 1/10 ratio of divalent Ge with Sb (Sb single doping) or with Ga + Sb (codoping of Ga and Sb), suppresses the hole concentration and, assuming a rigid band model, shifts the Fermi level (E_F) upwards, i.e., towards the conduction band (Figures 3b and 3c). We would like to mention that these statements must be considered with caution, as the theoretical calculations were performed based on a stoichiometric GeTe, where there is no Ge vacancy. But as found experimentally, GeTe always prefers to be in Te-rich composition and hence there exists some Ge vacancies. The p -type charge carriers still dominate the transport in Ga-Sb codoped GeTe, as observed from them the Hall measurement results (Table 1). The significant reduction in the carrier density indicates that the DOS at the Fermi-level will decrease and the E_F should be close to the gap for the Ga-Sb codoped GeTe. As per Boltzmann equation, such a scenario will obviously lead to an improved Seebeck coefficient, consistent with our experimental findings. Ga-Sb codoping adds donor states just below the conduction band of GeTe. Interestingly, we still found some Ga-induced resonant states in the top of the valence band when Sb was codoped to the Ge-Ga-Te system, but unlike the single doped $\text{Ge}_{1-x}\text{Ga}_x\text{Te}$, the resonant state was not near E_F in the Ga-Sb codoped system (Figure 3c).

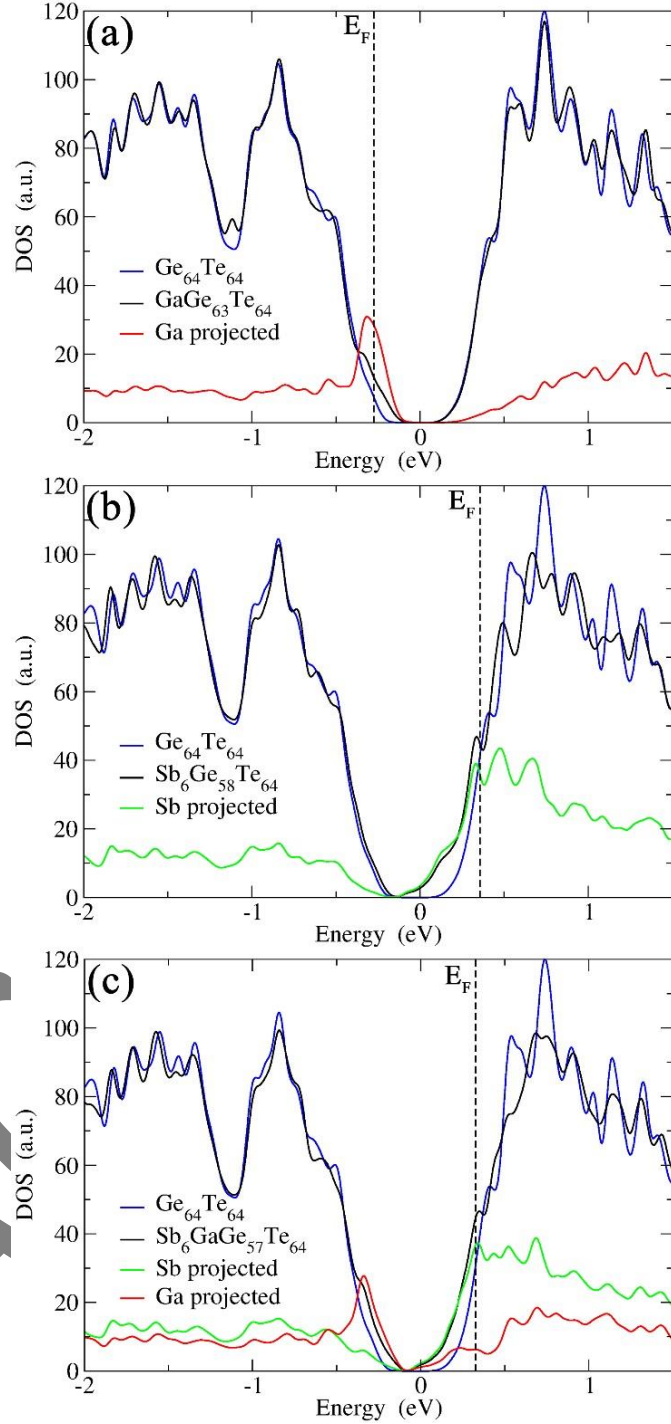


Figure 3. Calculated DOS for (a) $\text{GaGe}_{63}\text{Te}_{64}$ ($\text{Ge}_{0.98}\text{Ga}_{0.02}\text{Te}$), (b) $\text{Sb}_6\text{Ge}_{58}\text{Te}_{64}$ ($\text{Sb}_{0.09}\text{Ge}_{0.91}\text{Te}$) (c) $\text{GaSb}_6\text{Ge}_{57}\text{Te}_{64}$ ($\text{Ga}_{0.02}\text{Sb}_{0.09}\text{Ge}_{0.89}\text{Te}$) models (derived from the high temperature cubic GeTe phase). The DOS of each model is compared with that of the pristine cubic phase $\text{Ge}_{64}\text{Te}_{64}$ (GeTe). The Fermi level (E_F) of pristine GeTe is set arbitrarily at 0 eV. Green and red curves represent Sb and Ga projections. The dashed line represents the shifted Fermi level for the doped compositions. Additional Gaussian smearing of 25 meV was applied and the Ga projected DOS was magnified for a better readability of the curves.

The electronic band structures of the undoped, doped and codoped compositions were also computed and analyzed, hoping to provide useful insight on how the valence band structure is modified upon doping. They are plotted in Figure 4 along some high symmetry lines of the cubic Brillouin zone (BZ). From the electronic band structure of GeTe (Figures 4b and 4c), the direct band gap was calculated to be 225 meV at Γ point, which is in agreement with the literature.^{49,66} GeTe exhibits a second maximum of the valence band in the $\Gamma \rightarrow K (\Sigma)$ direction. The energy difference between light and heavy hole valence bands ($\Delta E_{L\bar{X}}$) for undoped cubic Ge₆₄Te₆₄ was found to be 64 meV, consistent with a recent report.⁶⁶ This $\Delta E_{L\bar{X}}$ value for c-GeTe is much lower when compared to that of the low temperature r-GeTe ($\Delta E_{L\bar{X}} = 150$ meV).⁶⁶ This is advantageous and is in agreement with the fact that the temperature increases the band convergence in GeTe.³⁸ As mentioned before, the ferroelectric structural transition was more favored with the codoping of Ga-Sb, since the transition temperature was reduced (SI, Figure S2). This structural strain relaxation from rhombohedral low symmetry (*R3m*) to cubic high symmetry (*Fm-3m*) will increase the electronic band valley degeneracy, a key factor for enhancing the Seebeck coefficient. Thus, codoping of Ga-Sb to GeTe promotes band valley convergence.

When 2 mol% Ga was added to GeTe, i.e., for (Ge_{0.98}Ga_{0.02}Te), the new impurity band arising from Ga states reduced the gap at Γ point to 66 meV (Figure 4d). The impurity states were located at the top of the valence band and extended somewhat within the gap. For 8-10 mol% Sb doping in GeTe, i.e. Sb₆Ge₅₈Te₆₄ (Sb_{0.09}Ge_{0.91}Te), the Sb states were located at the bottom of the conduction band (Figure 4e). The gap at Γ point decreased to 71 meV, while $\Delta E_{L\bar{X}}$ remained unchanged when compared to that of undoped GeTe, in agreement with the predictions made by Hong *et al.*⁶⁶ With 2 mol% Ga and 8 mol% Sb codoping in GeTe, i.e. GaSb₆Ge₅₇Te₆₄ (Ga_{0.02}Sb_{0.08}Ge_{0.90}Te), the gap at Γ point opened up (~ 165 meV). The presence of Sb and Ga modified the electronic band structure by activating the hole pockets at the bottom of the conduction band. The effective mass, m^* , associated with these hole pockets became larger (Table 1). These m^* values were calculated from Seebeck coefficient and carrier density and based on a single parabolic band, where acoustic phonon scatterings only were considered (see computational details in SI). Indeed, the m^* value for pristine GeTe was calculated to be $1.30m_e$ ($m_e =$ free electron mass) and it markedly increased to $2.38m_e$ for the Sb-Ga codoped Ga_{0.02}Sb_{0.08}Ge_{0.90}Te sample. This points towards an enhanced valence band degeneracy, which could explain the improved thermopower. More importantly, Ga-Sb codoping in GeTe promoted valence band convergence by strikingly reducing the energy separation between the light hole and heavy hole valence bands, $\Delta E_{L\bar{X}}$, to 26 meV (60% reduction in $\Delta E_{L\bar{X}}$ when compared to pristine GeTe). In this Ga-Sb codoped GeTe, the predominant contribution for the top of the valence band comes from Ga (Figure 4f vs. Figure 4h), indicating that it is not just Sb, but also Ga (of course together with Sb) that played a crucial role in promoting the valence band convergence in Ga_{0.02}Sb_{0.08}Ge_{0.90}Te. Thus, our calculations indicate a significant interaction between the substituted Ga and Sb atoms, and the codoping of Ga-Sb to GeTe though it did not position the resonance state at a favorable location near E_F , enhanced the valence band convergence besides pushing the system towards cubic (band degeneracy). All of this has helped to achieve a high Seebeck coefficient in Ga-Sb coped GeTe. The synergy achieved between these different band effects via codoping is the prime factor behind the impressive thermoelectric performance of Ge_{1-x-y}Ga_xSb_yTe.

As a matter of fact, as resonant states distort the DOS and reduces the band gap, only a low level of Ga doping (not more than 2 mol%) is beneficial, whereas band convergence is a tuning of the periodical band structure, and hence a relatively high Sb doping (8-10 mol%) and low Ga doping was required to influence the k -space band dispersion. Refer SI (Figure S7), where we have showed that an equal proportion doping of Ga and Sb was not beneficial.

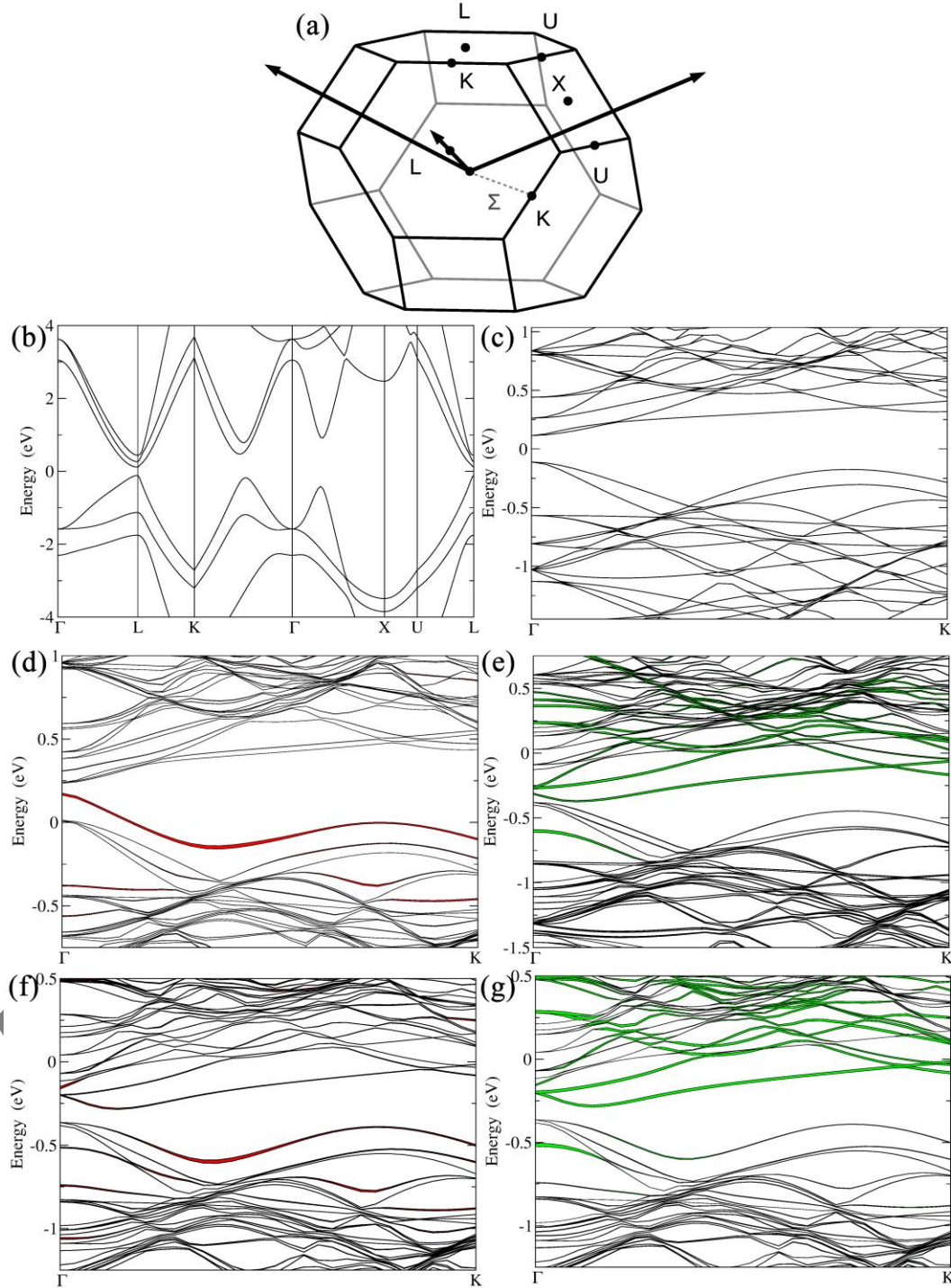


Figure 4. (a) Brillouin zone of *c*-GeTe. The band structures for (b) *c*-GeTe with primitive unit cell; (c) *c*-Ge₆₄Te₆₄ using a 4 × 4 × 4 supercell showing band folding in the $\Gamma \rightarrow K$ (Σ) direction. (d) GaGe₆₃Te₆₄ (*Ge*_{0.98}*Ga*_{0.02}Te) (e) Sb₆Ge₅₈Te₆₄ (*Sb*_{0.09}*Ge*_{0.91}Te); (f) GaSb₆Ge₅₇Te₆₄ (*Ga*_{0.02}*Sb*_{0.09}*Ge*_{0.89}Te) highlighting Ga projections and (g) GaSb₆Ge₅₇Te₆₄ (*Ga*_{0.02}*Sb*_{0.09}*Ge*_{0.89}Te) highlighting Sb projections. Line thickness is proportional to the projection of the wave function on the Ga (in red) and Sb (in green) orbitals.

More recently, a novel sintering process called ‘Flash-SPS’, a derivative of the flash and SPS sintering techniques has generated a lot of interest as it has been shown to improve the thermoelectric performance of Mg-Si based materials.⁶⁸ During normal SPS (which involves direct Joule heating of electrically conductive dies, usually graphite), the heating rate typically used is ~ 100 °C/min, whereas the flash technique employs thermal runaway to achieve ultra-fast sintering with heating rate as high as $\sim 10,000$ °C/min, producing dense materials in a matter of few seconds.^{69–71} An additional advantage of the flash-SPS method is that no preheating is required when conducting samples are used. Though flash sintering has been used predominantly to process high temperature ceramics like SiC,^{71,72} ZrO₂,⁶⁹ ZrB₂,⁷³ it has not been tried on many thermoelectric materials. Just recently, we have shown how to improve the TE properties of PbTe-based materials by the so called ‘Hybrid Flash-SPS’ processing.⁵³ Motivated by those results, we have extended that process to Ga and Sb codoped GeTe. Indeed, Ge_{0.90}Ga_{0.02}Sb_{0.08}Te was consolidated by ‘Hybrid’ Flash-SPS processing, where the powders were sintered at 893 K with a heating rate of $\sim 10,000$ °C/min (heated from 293 – 893 K in 3 seconds) under an axial pressure of 55 MPa. Typically, during a Flash-SPS process, the green compact sample was sandwiched between two graphite punches without a die and inserted in between the pistons of the SPS furnace.⁶⁸ But the ‘Hybrid’ Flash-SPS processing route is a variant of the originally developed Flash-SPS method, involving the use of a thin, low thermal inertia metal die to contain the TE powder during sintering.^{52,53} The schematics of the experimental set-up and the current flow paths are available in SI (Figure S1). Highly dense disk-shaped pellets were obtained with theoretical densities of $\sim 98\%$ for Hybrid Flash-SPS.

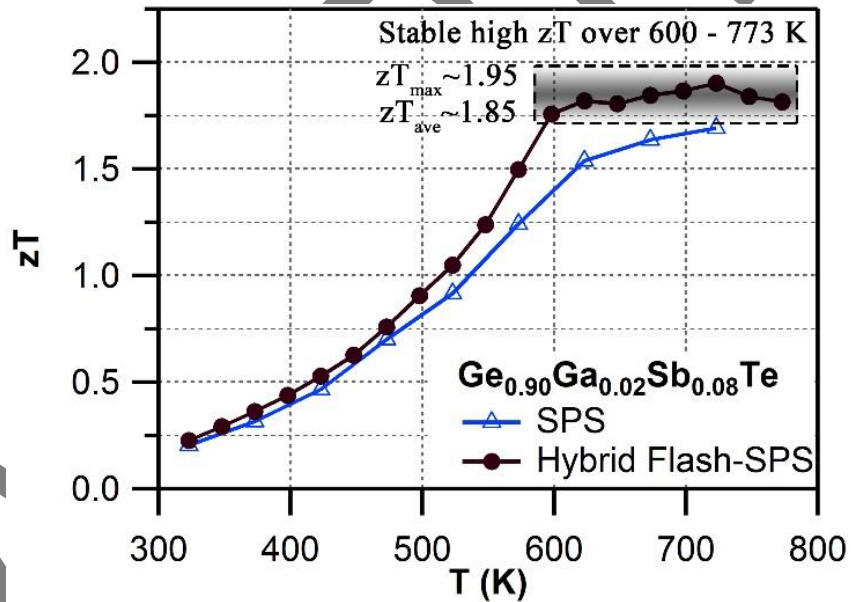


Figure 5. Temperature dependent zT for SPS Vs Hybrid Flash-SPS processed Ge_{0.90}Ga_{0.02}Sb_{0.08}Te sample.

It was established that higher the ratio of the carrier mobility to lattice thermal conductivity, the greater zT .⁷⁴ Normally, there is a trade-off when alloying a material. The lattice thermal conductivity is decreased due to scattering from impurities, but that also reduces the carrier mobility, meaning limited change in zT . An improvement in zT for an alloy system occurs only when κ_{latt} is reduced by a significant factor with little or no degradation of μ . It was found that hybrid flash-SPS processing enhanced the thermopower by suppressing the charge carrier density, without affecting the carrier mobility (see Table 1). For the sintered codoped samples, the hybrid flash-SPS sample in particular exhibited a mean low $\kappa_{latt} \sim 0.6$ in the temperature range from 550 K to 773 K (SI, Figure S8f). This reduction in κ_{latt} during flash processing is consistent with our recent report,⁵³ where we have shown that the ultra-fast sintering rate

achieved during hybrid flash-SPS processing has helped to reduce the grain growth and enhance the boundary scattering of heat carrying phonons at the intergrain region. Due to its lowered charge carrier density, the hybrid flash-SPS sample exhibited a lower σ when compared to the SPS sample (SI, Figure S8a), but this was well compensated for by the improvement in the Seebeck coefficient (SI, Figure S8b) and a significant reduction in κ_e (SI, Figure S8e). This has helped the hybrid flash-SPS sample to exhibit ultra-low $\kappa_{total} \sim 1$ at around 600 K (SI, Figure S8d). The enhanced thermopower coupled with the reduced electronic and lattice contributions to the thermal conductivity with no degradation in carrier mobility has helped the hybrid flash-SPS sample to reach a peak $zT \sim 1.95$ at 723 K (Figure 5). The hybrid flash-SPS sample crossed $zT > 1.75$ at a temperature as low as 600 K (whereas the SPS sample exhibited its peak $zT \sim 1.75$ only at 723 K), thus making it more suitable for mid-temperature practical applications. More importantly, the hybrid flash SPS sample maintained (almost stabilized) the high zT over a wide temperature range (from 600 K – 773 K). From a practical point of view, it is not the maximum zT (zT_{max}), but it is the average zT (zT_{ave}) value that determines the overall efficiency of a TE module. In this temperature range from 600 – 773 K, the zT was almost constant ($zT_{ave} \sim 1.85$ in the temperature range from 600 – 773 K), thus making it one of the best reported materials among the Pb-free GeTe family. The results obtained were consistent and reproducible during the heating and cooling cycles. With the hybrid flash-SPS sintering process, we have demonstrated that it is possible to optimize the charge carrier density, and at the same time benefit from the decreased thermal conductivity without significantly affecting the carrier mobility (i.e., higher μ/κ_{total} ratio). Moving forward, the hybrid flash-SPS technique can potentially be used as a strategic processing route to decouple electrical and thermal transport properties to produce high zT materials.

4. Conclusion

In summary, on the basis of our experimental and theoretical studies, we conclude that optimized codoping of Ga-Sb in c-GeTe induces multiple effects: (i) suppression of p -type charge carriers; (ii) activation of several bands with larger effective mass in the transport; (iii) reduction of the structural transition temperature and enhancement of band degeneracy; (iv) convergence of light and heavy hole valence bands; (v) Ga contributes predominantly to the top of the valence band (and thus Ga together with Sb promoting band convergence), despite the Ga-induced resonance state not at a favorable position near Fermi-level. These cooperative (synergistic) effects, combined with the benefits of hybrid flash-SPS processing, i.e., improvement of thermopower and reduction of thermal transport without any degradation in carrier mobility, helped to achieve remarkably high and stabilized zT values (close to 2 for $\text{Ge}_{0.90}\text{Ga}_{0.02}\text{Sb}_{0.08}\text{Te}$ for instance, i.e. an improvement by 110% compared to undoped c-GeTe), making these Ga-Sb co-doped GeTe materials ideal candidates for mid-temperature power generation.

Acknowledgement

The European Commission's Horizon 2020 research and innovation program under Marie Skłodowska-Curie GA.642557 (CoACH-ETN) is gratefully acknowledged for financial support. Dr. Sylvain Tricot (IPR, Rennes) is acknowledged for his assistance in collecting Hall measurement data.

References

- 1 J. R. Sootsman, H. Kong, C. Uher, J. J. D'Angelo, C.-I. Wu, T. P. Hogan, T. Caillat and M. G. Kanatzidis, *Angew. Chem. Int. Ed.*, 2008, **47**, 8618–8622.
- 2 X. Su, P. Wei, H. Li, W. Liu, Y. Yan, P. Li, C. Su, C. Xie, W. Zhao, P. Zhai, Q. Zhang, X. Tang and C. Uher, *Adv. Mater.*, 2017, **29**, 1602013.
- 3 Y. Zheng, Q. Zhang, X. Su, H. Xie, S. Shu, T. Chen, G. Tan, Y. Yan, X. Tang, C. Uher and G. J. Snyder, *Adv. Energy Mater.*, 2015, **5**, 1401391.
- 4 D. T. Morelli, V. Jovovic and J. P. Heremans, *Phys. Rev. Lett.*, 2008, **101**, 035901.
- 5 M. K. Jana and K. Biswas, *ACS Energy Lett.*, 2018, **3**, 1315–1324.
- 6 M. Samanta, K. Pal, P. Pal, U. V. Waghmare and K. Biswas, *J. Am. Chem. Soc.*, 2018, **140**, 5866–5872.
- 7 B. C. Sales, D. Mandrus and R. K. Williams, *Science*, 1996, **272**, 1325–1328.
- 8 A. Banik, U. S. Shenoy, S. Anand, U. V. Waghmare and K. Biswas, *Chem. Mater.*, 2015, **27**, 581–587.
- 9 Y. Pei, X. Shi, A. LaLonde, H. Wang, L. Chen and G. J. Snyder, *Nature*, 2011, **473**, 66–69.
- 10 L. D. Hicks and M. S. Dresselhaus, *Phys. Rev. B*, 1993, **47**, 12727–12731.
- 11 J. M. O. Zide, D. Vashaee, Z. X. Bian, G. Zeng, J. E. Bowers, A. Shakouri and A. C. Gossard, *Phys. Rev. B*, 2006, **74**, 205335.
- 12 Q. Zhang, B. Liao, Y. Lan, K. Lukas, W. Liu, K. Esfarjani, C. Opeil, D. Broido, G. Chen and Z. Ren, *Proc. Natl. Acad. Sci. U. S. A.*, 2013, **110**, 13261–13266.
- 13 S. Lin, W. Li, Z. Chen, J. Shen, B. Ge and Y. Pei, *Nat. Commun.*, 2016, **7**, 10287.
- 14 M. S. Dresselhaus, G. Chen, M. Y. Tang, R. G. Yang, H. Lee, D. Z. Wang, Z. F. Ren, J.-P. Fleurial and P. Gogna, *Adv. Mater.*, 2007, **19**, 1043–1053.
- 15 H. Wang, Y. Pei, A. D. LaLonde and G. J. Snyder, *Proc. Natl. Acad. Sci.*, 2012, **109**, 9705–9709.
- 16 Y. Pei, A. D. LaLonde, H. Wang and G. J. Snyder, *Energy Environ. Sci.*, 2012, **5**, 7963–7969.
- 17 P. Lucas, C. Conseil, Z. Yang, Q. Hao, S. Cui, C. Boussard-Pledel, B. Bureau, F. Gascoin, C. Caillaud, O. Gulbiten, T. Guizouarn, P. Baruah, Q. Li and J. Lucas, *J. Mater. Chem. A*, 2013, **1**, 8917–8925.
- 18 B. Srinivasan, S. Cui, C. Prestipino, A. Gellé, C. Boussard-Pledel, S. Ababou-Girard, A. Trapananti, B. Bureau and S. Di Matteo, *J. Phys. Chem. C*, 2017, **121**, 14045–14050.
- 19 B. Srinivasan, C. Boussard-Pledel, V. Dorcet, M. Samanta, K. Biswas, R. Lefèvre, F. Gascoin, F. Cheviré, S. Tricot, M. Reece and B. Bureau, *Materials*, 2017, **10**, 328.
- 20 A. P. Gonçalves, E. B. Lopes, G. Delaizir, J. B. Vaney, B. Lenoir, A. Piarristeguy, A. Pradel, J. Monnier, P. Ochin and C. Godart, *J. Solid State Chem.*, 2012, **193**, 26–30.
- 21 R. Al Rahal Al Orabi, N. A. Mecholsky, J. Hwang, W. Kim, J.-S. Rhyee, D. Wee and M. Fornari, *Chem. Mater.*, 2016, **28**, 376–384.
- 22 A. Banik, U. S. Shenoy, S. Saha, U. V. Waghmare and K. Biswas, *J. Am. Chem. Soc.*, 2016, **138**, 13068–13075.
- 23 L. Wang, X. Tan, G. Liu, J. Xu, H. Shao, B. Yu, H. Jiang, S. Yue and J. Jiang, *ACS Energy Lett.*, 2017, **2**, 1203–1207.
- 24 A. Banik, S. Roychowdhury and K. Biswas, *Chem. Commun.*, 2018, **54**, 6573–6590.
- 25 B. Srinivasan, C. Boussard-Pledel and B. Bureau, *Mater. Lett.*, 2018, **230**, 191–194.
- 26 D. Birc, S. D. Mahanti, E. Quarez, K.-F. Hsu, R. Pcionek and M. G. Kanatzidis, *Phys. Rev. Lett.*, 2004, **93**, 146403.
- 27 Q. Zhang, F. Cao, W. Liu, K. Lukas, B. Yu, S. Chen, C. Opeil, D. Broido, G. Chen and Z. Ren, *J. Am. Chem. Soc.*, 2012, **134**, 10031–10038.
- 28 B. Srinivasan, F. Gucci, C. Boussard-Pledel, F. Cheviré, M. J. Reece, S. Tricot, L. Calvez and B. Bureau, *J. Alloys Compd.*, 2017, **729**, 198–202.
- 29 C. Fu, S. Bai, Y. Liu, Y. Tang, L. Chen, X. Zhao and T. Zhu, *Nat. Commun.*, 2015, **6**, 8144.
- 30 W. Liu, X. Tan, K. Yin, H. Liu, X. Tang, J. Shi, Q. Zhang and C. Uher, *Phys. Rev. Lett.*, 2012, **108**, 166601.

- 31 S. H. Yang, T. J. Zhu, T. Sun, J. He, S. N. Zhang and X. B. Zhao, *Nanotechnology*, 2008, **19**, 245707.
- 32 T. Schröder, S. Schwarzmüller, C. Stiewe, J. de Boor, M. Hölzel and O. Oeckler, *Inorg. Chem.*, 2013, **52**, 11288–11294.
- 33 T. Schröder, T. Rosenthal, N. Giesbrecht, S. Maier, E.-W. Scheidt, W. Scherer, G. J. Snyder, W. Schnick and O. Oeckler, *J. Mater. Chem. A*, 2014, **2**, 6384–6395.
- 34 M. Samanta, S. Roychowdhury, J. Ghatak, S. Perumal and K. Biswas, *Chem. Eur. J.*, 2017, **23**, 7438 – 7443
- 35 F. Fahrnbauer, D. Souchay, G. Wagner and O. Oeckler, *J. Am. Chem. Soc.*, 2015, **137**, 12633–12638.
- 36 Y. Gelbstein and J. Davidow, *Phys. Chem. Chem. Phys.*, 2014, **16**, 20120–20126.
- 37 S. Perumal, S. Roychowdhury and K. Biswas, *Inorg. Chem. Front.*, 2016, **3**, 125–132.
- 38 D. Wu, L.-D. Zhao, S. Hao, Q. Jiang, F. Zheng, J. W. Doak, H. Wu, H. Chi, Y. Gelbstein, C. Uher, C. Wolverton, M. Kanatzidis and J. He, *J. Am. Chem. Soc.*, 2014, **136**, 11412–11419.
- 39 L. Wu, X. Li, S. Wang, T. Zhang, J. Yang, W. Zhang, L. Chen and J. Yang, *NPG Asia Mater.*, 2017, **9**, e343.
- 40 L. Yang, J. Q. Li, R. Chen, Y. Li, F. S. Liu and W. Q. Ao, *J. Electron. Mater.*, 2016, **45**, 5533–5539.
- 41 S. Perumal, S. Roychowdhury, D. S. Negi, R. Datta and K. Biswas, *Chem. Mater.*, 2015, **27**, 7171–7178.
- 42 E. Nshimiyimana, X. Su, H. Xie, W. Liu, R. Deng, T. Luo, Y. Yan and X. Tang, *Sci. Bull.*, 2018, **63**, 717–725.
- 43 B. Srinivasan, R. Gautier, F. Gucci, B. Fontaine, J.-F. Halet, F. Cheviré, C. Boussard-Pledel, M. J. Reece and B. Bureau, *J. Phys. Chem. C*, 2018, **122**, 227–235.
- 44 Z. Zheng, X. Su, R. Deng, C. Stoumpos, H. Xie, W. Liu, Y. Yan, S. Hao, C. Uher, C. Wolverton, M. G. Kanatzidis and X. Tang, *J. Am. Chem. Soc.*, 2018, **140**, 2673–2686.
- 45 J. K. Lee, M. W. Oh, B. S. Kim, B. K. Min, H. W. Lee and S. D. Park, *Electron. Mater. Lett.*, 2014, **10**, 813–817.
- 46 Y. Rosenberg, Y. Gelbstein and M. P. Dariel, *J. Alloys Compd.*, 2012, **526**, 31–38.
- 47 J. Li, X. Zhang, S. Lin, Z. Chen and Y. Pei, *Chem. Mater.*, 2017, **29**, 605–611.
- 48 M. Samanta and K. Biswas, *J. Am. Chem. Soc.*, 2017, **139**, 9382–9391.
- 49 S. Perumal, P. Bellare, U. S. Shenoy, U. V. Waghmare and K. Biswas, *Chem. Mater.*, 2017, **29**, 10426–10435.
- 50 J. Li, X. Zhang, Z. Chen, S. Lin, W. Li, J. Shen, I. T. Witting, A. Faghaninia, Y. Chen, A. Jain, L. Chen, G. J. Snyder and Y. Pei, *Joule*, 2018, **2**, 976–987.
- 51 S. Perumal, S. Roychowdhury and K. Biswas, *J. Mater. Chem. C*, 2016, **4**, 7520–7536.
- 52 F. Gucci, T. G. Saunders and M. J. Reece, *Scr. Mater.*, 2018, **157**, 58–61.
- 53 B. Srinivasan, B. Fontaine, F. Gucci, V. Dorcet, T. G. Saunders, M. Yu, F. Cheviré, C. Boussard-Pledel, J.-F. Halet, R. Gautier, M. J. Reece and B. Bureau, *Inorg. Chem.*, 2018, Inpress.
[DOI: 10.1021/acs.inorgchem.8b02248](https://doi.org/10.1021/acs.inorgchem.8b02248)
- 54 H.-S. Kim, Z. M. Gibbs, Y. Tang, H. Wang and G. J. Snyder, *APL Mater.*, 2015, **3**, 041506.
- 55 L. Zhang, J. Wang, Z. Cheng, Q. Sun, Z. Li and S. Dou, *J. Mater. Chem. A*, 2016, **4**, 7936–7942.
- 56 G. Kresse and D. Joubert, *Phys. Rev. B*, 1999, **59**, 1758–1775.
- 57 G. Kresse and J. Furthmüller, *Phys. Rev. B*, 1996, **54**, 11169–11186.
- 58 J. P. Perdew, K. Burke and M. Ernzerhof, *Phys. Rev. Lett.*, 1996, **77**, 3865–3868.
- 59 K. Hoang, S. D. Mahanti and M. G. Kanatzidis, *Phys. Rev. B*, 2010, **81**, 115106.
- 60 A. F. May, E. S. Toberer, A. Saramat and G. J. Snyder, *Phys. Rev. B*, 2009, **80**, 125205.
- 61 E. S. Toberer, A. Zevalkink, N. Crisosto and G. J. Snyder, *Adv. Funct. Mater.*, 2010, **20**, 4375–4380.
- 62 E. M. Levin, M. F. Besser and R. Hanus, *J. Appl. Phys.*, 2013, **114**, 083713.
- 63 E. M. Levin, *Phys. Rev. B*, 2016, **93**, 045209.
- 64 J. Androulakis, I. Todorov, D.-Y. Chung, S. Ballikaya, G. Wang, C. Uher and M. Kanatzidis, *Phys. Rev. B*, 2010, **82**, 115209.
- 65 S. Roychowdhury, U. Sandhya Shenoy, U. V. Waghmare and K. Biswas, *J. Mater. Chem. C*, 2017, **5**, 5737–5748.

- 66 M. Hong, Z.-G. Chen, L. Yang, Y.-C. Zou, M. S. Dargusch, H. Wang and J. Zou, *Adv. Mater.*, **30**, 1705942.
- 67 H. Fritzsche, *Science*, 1972, **176**, 1117–1117.
- 68 B. Du, F. Gucci, H. Porwal, S. Grasso, A. Mahajan and M. J. Reece, *J. Mater. Chem. C*, 2017, **5**, 1514–1521.
- 69 Cologna Marco, Rashkova Borianna and Raj Rishi, *J. Am. Ceram. Soc.*, 2010, **93**, 3556–3559.
- 70 M. Yu, S. Grasso, R. Mckinnon, T. Saunders and M. J. Reece, *Adv. Appl. Ceram.*, 2017, **116**, 24–60.
- 71 E. A. Olevsky, S. M. Rolfing and A. L. Maximenko, *Sci. Rep.*, 2016, **6**, 33408.
- 72 S. Grasso, E.-Y. Kim, T. Saunders, M. Yu, A. Tudball, S.-H. Choi and M. Reece, *Cryst. Growth Des.*, 2016, **16**, 2317–2321.
- 73 Grasso Salvatore, Saunders Theo, Porwal Harshit, Cedillos-Barraza Omar, Jayaseelan Daniel Doni, Lee William E., Reece Mike John and Fahrenholtz W., *J. Am. Ceram. Soc.*, 2014, **97**, 2405–2408.
- 74 J. L. Wang, H. Wang, G. J. Snyder, X. Zhang, Z. H. Ni and Y. F. Chen, *J. Phys. Appl. Phys.*, 2013, **46**, 405301.

ACCEPTED